

**UNCLASSIFIED**

**AD 406 282** \_\_\_\_\_

**DEFENSE DOCUMENTATION CENTER**

**FOR**

**SCIENTIFIC AND TECHNICAL INFORMATION**

**CAMERON STATION, ALEXANDRIA, VIRGINIA**



**UNCLASSIFIED**

## **REPRODUCTION QUALITY NOTICE**

**This document is the best quality available. The copy furnished to DTIC contained pages that may have the following quality problems:**

- **Pages smaller or larger than normal.**
- **Pages with background color or light colored printing.**
- **Pages with small type or poor printing; and or**
- **Pages with continuous tone material or color photographs.**

**Due to various output media available these conditions may or may not cause poor legibility in the microfiche or hardcopy output you receive.**

☐

**If this block is checked, the copy furnished to DTIC contained pages with color printing, that when reproduced in Black and White, may change detail of the original copy.**

NOTICE: When government or other drawings, specifications or other data are used for any purpose other than in connection with a definitely related government procurement operation, the U. S. Government thereby incurs no responsibility, nor any obligation whatsoever; and the fact that the Government may have formulated, furnished, or in any way supplied the said drawings, specifications, or other data is not to be regarded by implication or otherwise as in any manner licensing the holder or any other person or corporation, or conveying any rights or permission to manufacture, use or sell any patented invention that may in any way be related thereto.

⑤ 150 700

①

63-3-6

AD No. 406 282

FILE COPY



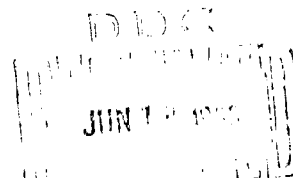
406 282

U. S. Army Ordnance  
Ballistics Research Laboratory  
Aberdeen Proving Ground, Maryland  
Approved Proposal No. 3175  
Authorization No. 4086

*Seal 1*

## EXPLOSIVES RESEARCH LABORATORY

### HYPERVELOCITY IMPACT PHENOMENA



Quarterly Report  
March 1, 1963 to May 31, 1963

BUREAU OF MINES, PITTSBURGH, PA.

*76*

UNITED STATES  
DEPARTMENT OF  
THE INTERIOR

*4,00*

④ NA  
⑤ 150 760  
(7-8) NA

⑥ HYPERVELOCITY IMPACT PHENOMENA

⑨ Quarterly Report.

March 1, 1963 to May 31, 1963.

Prepared for:

U. S. Army Ordnance  
Ballistic Research Laboratory  
Aberdeen Proving Ground, Maryland  
Approved Proposal No. 3175  
Authorization No. 4086

by

⑩ Richard W. Watson,  
Karl R. Becker,  
J. Edmund Hay and  
Frank C. Gibson .

Approved by:

  
Robert W. Van Dolah, Chief  
Explosives Research Laboratory

U. S. Department of the Interior  
Bureau of Mines  
Pittsburgh, Pa.  
June 6, 1963

(11) 6 June 63,

(12) 40 p.

(13) NA

(14) NA

(15) NA

(16) NA

(17) NA

(18) NA

(19) NA

(20) U

(21) NA

## HYPERVELOCITY IMPACT PHENOMENA

### Introduction

~~This report presents~~ a summation of the research performed at the Explosives Research Laboratory, Pittsburgh, Pa. in the field of hypervelocity impact on thin targets. <sup>is presented,</sup> The research is supported by U. S. Army Ordnance, Ballistic Research Laboratory, Aberdeen Proving Ground, Md. It is submitted in lieu of the regular quarterly report, for the period March 1, 1963 to May 31, 1963 and basically contains the information presented at the Sixth Hypervelocity Impact Symposium held in Cleveland, Ohio April 30 through May 2, 1963.

The immediate goal of the research is to obtain a complete description of the thin-plate perforation process within the limits of available explosive projectors. The bulk of the work to date has been carried out with 2024-T3 aluminum as the target material; however, other higher density target materials were used when required for clarification of impact pressure effects. Four basic categories characterize the results of target impact: primary target damage, the number distribution of spall particles, the mass distribution of spall and the velocity of the ejecta formed during the perforation process.

406282



## PROCEDURES AND DISCUSSION

### I. Survey of Impact Damage to Thin and Thick 2024-T3 Aluminum Targets

The research was carried out with two basic explosive projector systems, each of which is characterized by a different projectile mass. One projector, which will be referred to as Scale I, utilized cylindrical steel projectiles having a mass of  $0.0235 \pm 0.0005$  gram. The Scale I projectors can be further subdivided according to projectile velocities of 2.0 km/sec, 3.2 km/sec, and 4.0 km/sec; the latter two systems were developed by two of the authors (1)<sup>1/</sup> while associated with the Carnegie Institute of Technology. The projectiles were 1/16 inch long and 1/16 inch in diameter; the 2.0 km/sec and 3.2 km/sec projectiles were fabricated from Ketos steel drill rod of BHN 200; steel piano wire was used for the 4.0 km/sec projectile. The second projector, referred to as Scale II, provided a velocity of 3.2 km/sec for a projectile 1/8 inch long and 1/8 inch in diameter, weighing 0.187 gram, made of Ketos steel. The velocity range for the Scale II projectiles was increased by the use of an air-cavity projector designed at the Ballistic Research Laboratories (2); this projector propelled a 0.18 gram steel projectile at a velocity of 5.0 km/sec.

Thick or quasi-infinite targets are defined here as targets of such dimensions that no measurable change in final crater dimension

---

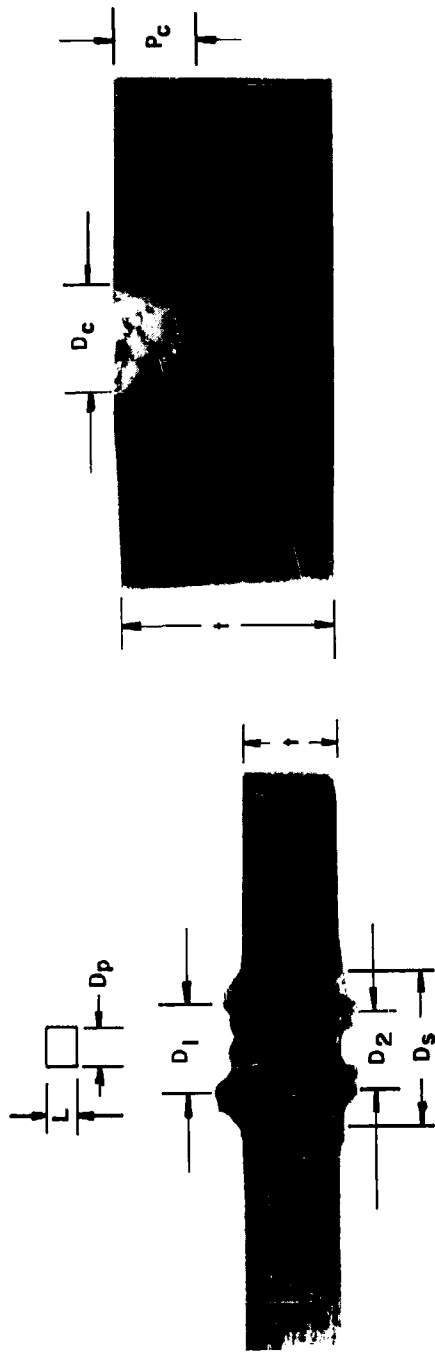
<sup>1/</sup> Underlined numbers in parentheses refer to items in the list of references at the end of this report.

is affected by increasing the size of the target. In tests with 2024-T3 aluminum, it was found that targets having a thickness equal to 3 to 4 times the crater depth and a surface area roughly 25 times that of the crater satisfied these conditions within the accuracy of the crater measurements. Since the research program was principally concerned with a description of behind-target effects, the term "thin target" is generally applied to any target capable of being perforated by a given projectile with a finite probability. For 2024-T3 aluminum, target thicknesses ranged from 3 to 4 times the projectile lengths over the velocity range investigated.

The pertinent variables recorded for thick targets were crater volume, crater depth, and crater diameter; for thin targets, they were entrance and exit diameters of the perforation. In cases where shock spallation was pronounced, the diameter of the spalled area on the back surface of the target was also recorded. The manner in which these variables are defined is illustrated in figure 1 where "thin" and "thick" targets, impacted with Scale II, 3.2 km/sec projectiles are shown.

The pertinent features of these measurements are presented in figures 2 through 7 and can be summarized as follows:

- (1) For thick targets, crater volume was found to be proportional to the kinetic energy of the projectile over the velocity range 2 km/sec to 5 km/sec. This is illustrated in figure 2 where crater volume per unit projectile energy is plotted as a function of impact velocity.



- $D_p$  - Projectile Diameter
- $L$  - Projectile Length
- $D_1$  - Perforation Entrance Diameter
- $D_2$  - Perforation Exit Diameter
- $D_s$  - Spall Diameter
- $t$  - Target Thickness
- $D_c$  - Crater Diameter
- $P_c$  - Crater Depth

FIGURE 1. - Features of a Thin Plate and a Crater Produced in a Thick Target.

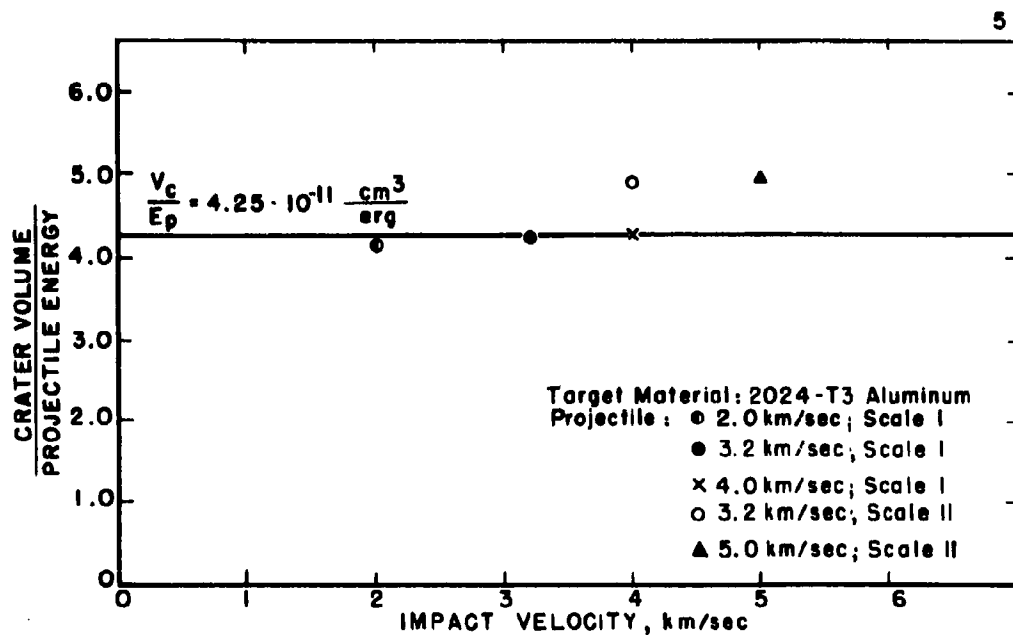


FIGURE 2. - Cratering Efficiency as a Function of Impact Velocity.

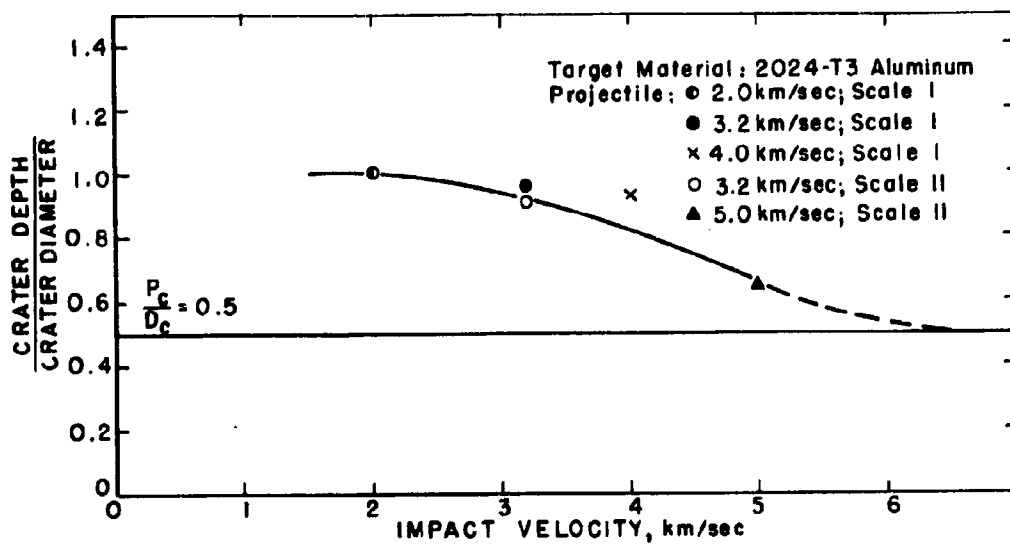


FIGURE 3. - Variation of Crater Shape with Impact Velocity.

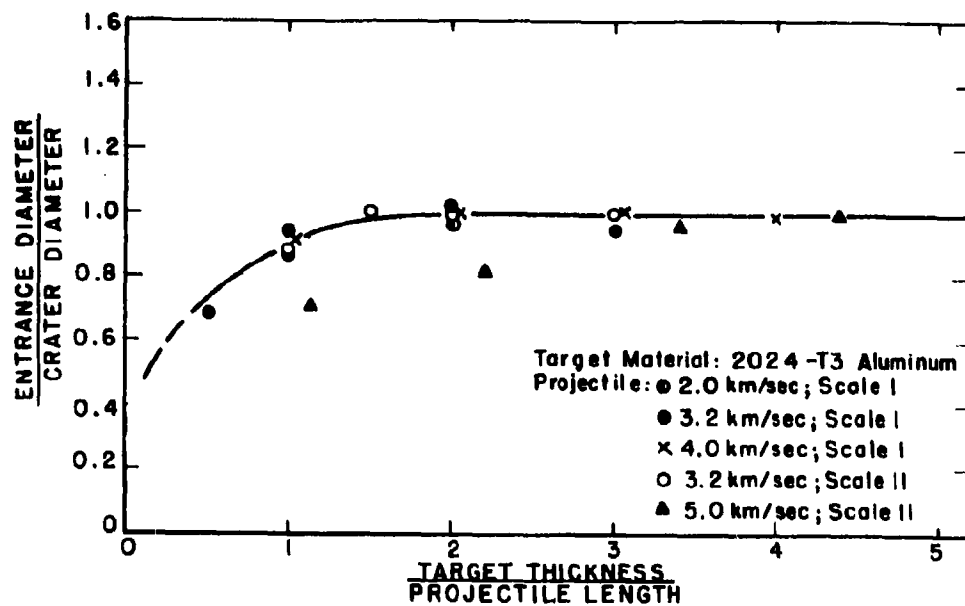


FIGURE 4.- Dependence of Perforation Entrance Diameter on Target Thickness.

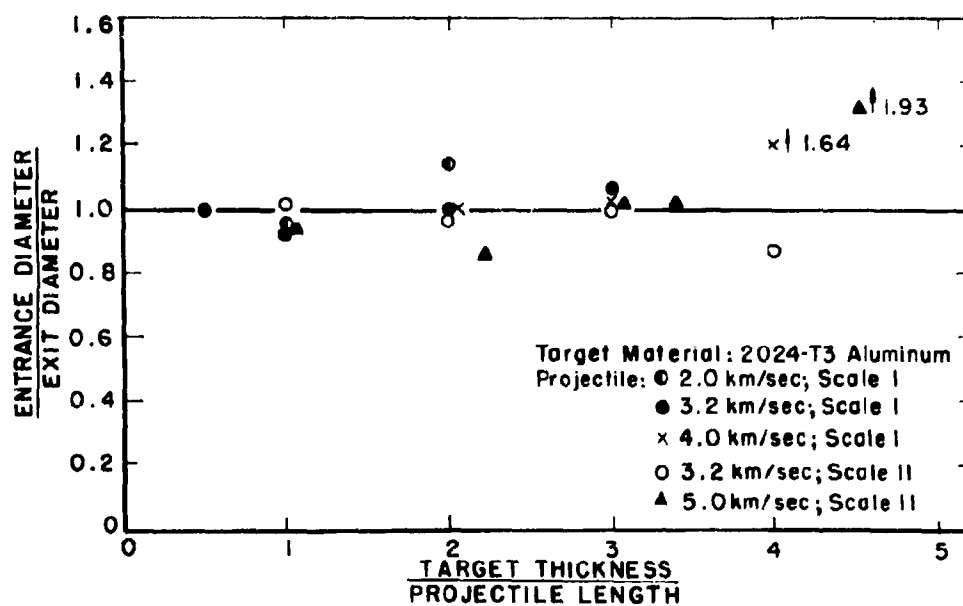


FIGURE 5.- Plot Showing Tendency for Perforations to be Cylindrical for Impacts Ranging from 2.0 to 5.0 km/sec.

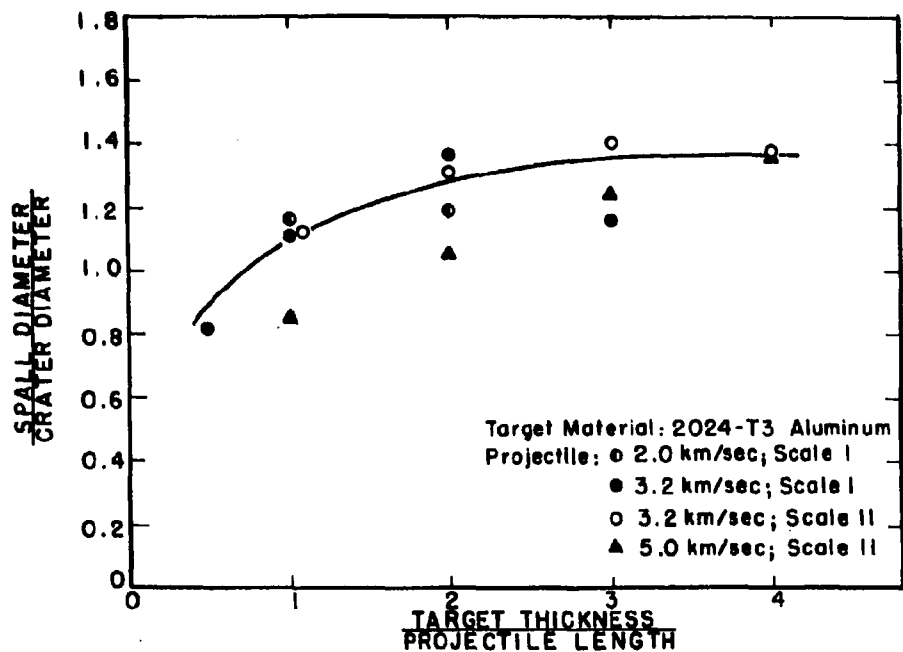


FIGURE 6.- Variation in Exit Spall Diameter with Target Thickness.

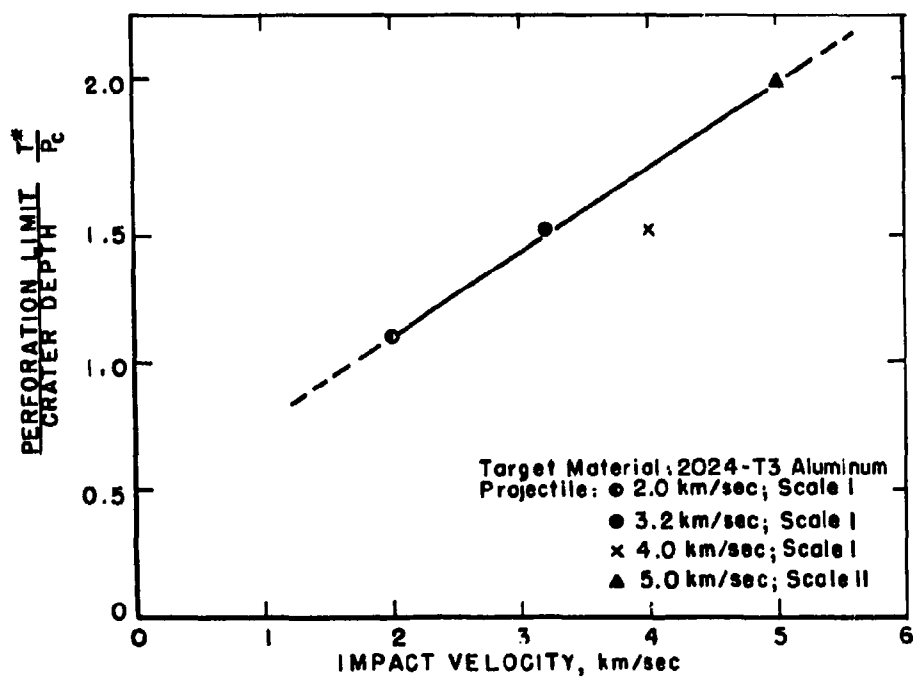


FIGURE 7.- Increase in Penetration Potential with Increasing Impact Velocity.

The apparent discrepancy for the Scale II projectiles can be attributed to the fact that appreciable front surface spallation occurred in these two cases, giving rise to large uncertainties in the volume determinations.

(2) At low impact velocities, the craters are narrow and deep while at velocities approaching the sonic velocity of the target material (5.1 km/sec) the craters approach a hemispherical shape. This is shown in figure 3 where the ratio of the crater depth to the crater diameter is plotted against the impact velocity. The volume-energy dependency and the observation concerning crater shape are in accord with the results of other investigations for the same range of impact velocities (3,4).

(3) For thin targets having thicknesses in excess of approximately 1.5 times the projectile length, the perforation entrance diameter is independent of target thickness; however, there is a noticeable decrease in entrance diameter for targets of lesser thickness. These features are illustrated in figure 4 where the ratios of the entrance diameters to the crater diameters are plotted as functions of reduced target thickness. Since, as illustrated in figure 5, the perforations are nearly cylindrical, these comments also apply to the exit diameters. The decrease in perforation entrance diameter with diminishing target thickness has been observed for a variety of target materials (5); it has been demonstrated that the perforation diameter for 2S-O aluminum approaches the projectile diameter for targets of thicknesses much less than the projectile length. The results with 2024-T3 aluminum targets show the same trend.

The dependence of exit spall diameter on target thickness is illustrated in figure 6 where the ratio of the spall diameter to the crater diameter is plotted as a function of reduced target thickness for different impact conditions. The results show that, in general, the spall diameter tends to increase with increasing target thickness over the velocity range investigated.

An important feature of these perforation studies is illustrated in figure 7 where, from a practical point of view, the difference in behavior between a thin target and a thick target is delineated. In this plot the ratio  $T^*/P_c$  is plotted as a function of impact velocity. The variable  $T^*$  is the target thickness for which the expectation of complete perforation by a given projectile becomes negligible;  $P_c$  is the crater depth in a semi-infinite target. Values of  $T^*$  for a given projectile-target combination were estimated from the perforation probabilities observed in targets having thicknesses of about  $T^*$ . No attempt was made to statistically determine the values of  $T^*$ ; however, the values used in figure 7 are probably accurate within  $\pm 5$  percent. The results show that the ratio  $T^*/P_c$  is a monotonically increasing function of the impact velocity, reaching values in excess of 1.5 for impacts in the 4.0 to 5.0 km/sec region. The significance of this observation is that the magnitude of crater depths in semi-infinite targets does not even closely approximate the penetration capabilities of the projectile through thin targets.

## II. Number Distribution

The term "number distribution" refers to the manner in which the spall particles, produced by projectile-target impacts, are spatially distributed behind the target. The experimental technique for determining the distribution is illustrated in figure 8. A witness foil, consisting of 1-mil thick aluminum supported by a backing of fiber-board, was located 6-1/2 inches beyond the target. The witness foil indicated the direction in which individual spall particles were propelled.

For purposes of analysis, the witness foil was mapped out in a family of concentric circles whose origin is located on a line through the perforation and normal to the target surface. The number of perforations, found in an element of area,  $\Delta r \Delta \phi$ , were counted and weighted by the reciprocal of the intercepted solid angle element,  $\Delta \Omega$ . The weighted count thus has the dimensions - number of fragments per unit solid angle and may be interpreted as representing the population density for a particular solid angle element. The total number of particles (N) is a function of the target thickness, the projectile velocity, and the projectile scale size. A complete reduction of all data at normal incidence is possible if the population density for each impact data set is multiplied by the factor  $\frac{1}{N}$ . Thus, the term  $\left(\frac{1}{N} \frac{\Delta N}{\Delta \Omega}\right)$  expresses the density of a given element of solid angle as a fraction of the total population.

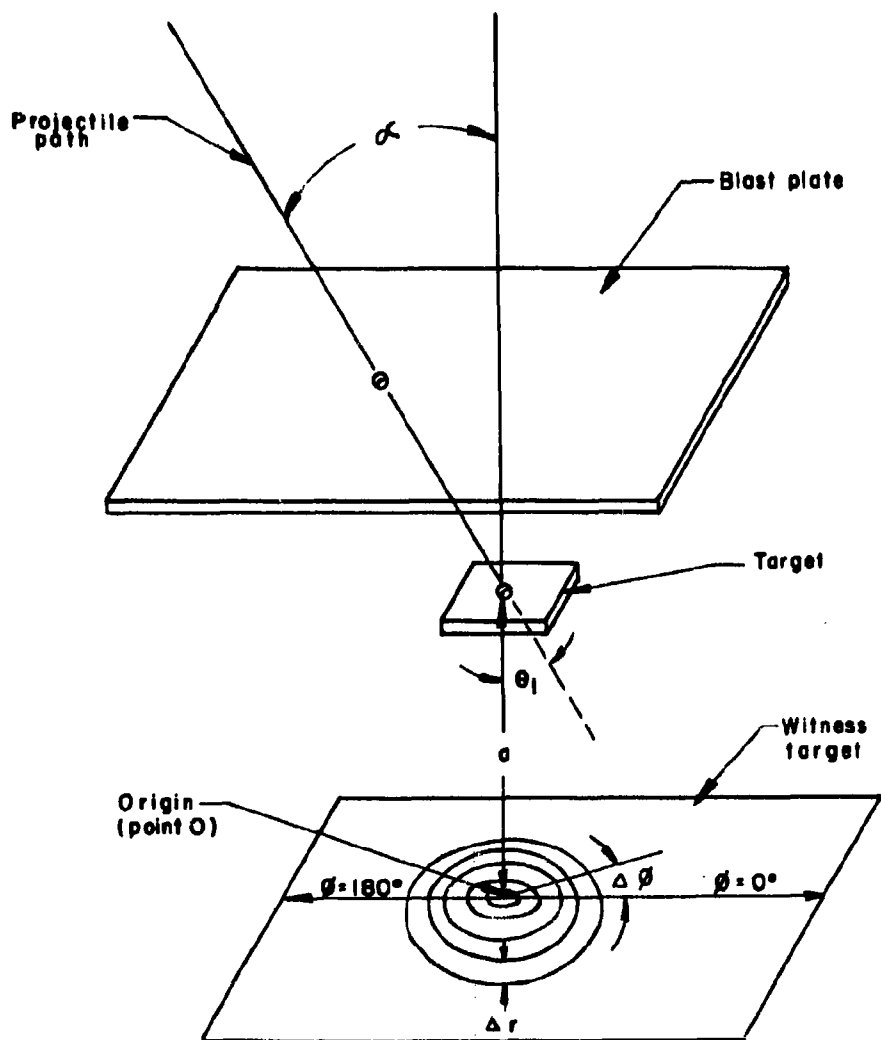


FIGURE 8.- Experimental Set-up for Determining the Spatial Distribution of Spill Fragments.

Number distributions have been determined for impacts on various thicknesses of 2024-T3 aluminum targets with both Scale I and Scale II projectiles over the velocity range 2 km/sec to 5 km/sec. These data are presented in figure 9 which shows  $\frac{1}{N} \left( \frac{\Delta N}{\Delta \Omega} \right)$  vs  $\Omega$  where  $\Omega$  is a measure of the radial distance from the center of impact. Each data set is an average of several target thicknesses because the distributions for individual target thicknesses did not vary more than the experimental error. Within reasonable limits, the six data sets define one curve; the significance of this is that the percentage of the total number of spall particles found in corresponding elements of space is independent of projectile scale size, target thickness, and projectile velocity. The data for 3.2 km/sec, Scale I projectiles, are from an earlier paper (5); in this work, the normalized distributions for 2024-T3 aluminum, 2S-O aluminum, magnesium, and lead were found to be essentially the same. Another significant feature of the data deals with the distribution for spall particles having higher penetration capabilities. Data points for these superior particles are identified by stars and are shown to fit the curve as well as any other data point set. The superior group was separated from the aggregate group by filtering out the inferior particles with an additional 7 mils of aluminum foil; about 20 percent of the total population penetrated the filter.

The experimental technique, mentioned earlier, involved counting holes in witness targets and did not provide a distinction between

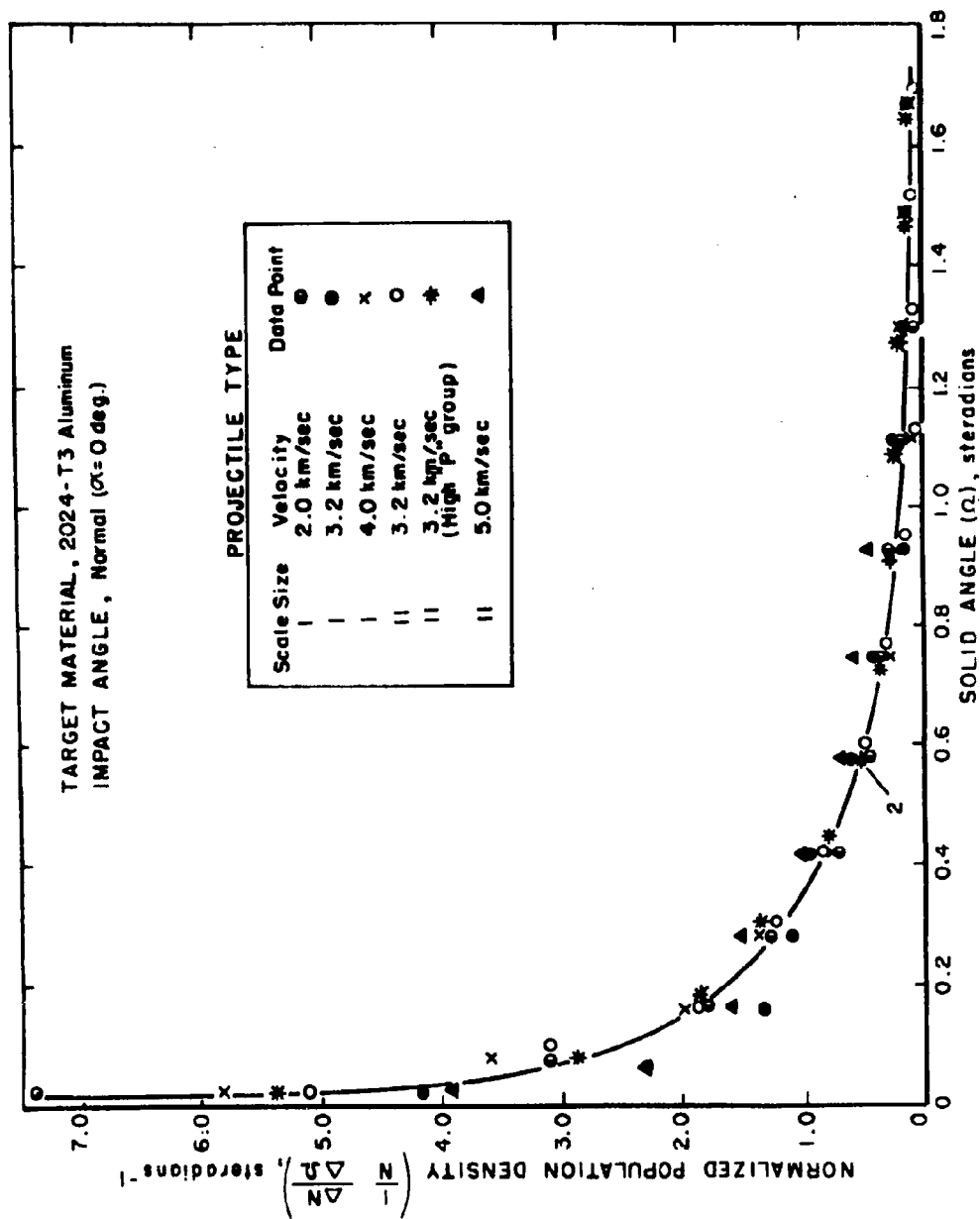


FIGURE 9.- Relationship Between Normalized Spall Numbers and Radial Distance from the Center of Spall Impact

projectile remnants and target spall particles. The desirability of establishing separate distributions for the two types of particles required analyses by a somewhat more time-consuming technique. A pan of gelatin was substituted for the aluminum witness foil; the gelatin layer was cut, after the impact event, into concentric, annular rings and each ring of gelatin was then dissolved in hot water and the individual particles recovered by filtration. The projectile remnants (steel) are separated magnetically from the target particles (aluminum) and counted. Distribution curves from tests using this technique are shown in figures 10 and 11 for the number of target spall particles and number of projectile remnants respectively.

The two figures show data for three different projectile parameters and illustrate several important points: (1) the percentage of the total number of target spall particles or total number of projectile remains found in a given space element is independent of projectile scale size, projectile velocity, or target thickness; (2) compared to the projectile remains, the target spall particles have a greater tendency to be radially dispersed.

Another interesting feature of these data is the effect of projectile scale size upon the total number of particles produced. The effect is shown in figure 12 for Scale I and Scale II projectiles impacting various thicknesses of 2024-T3 aluminum targets at 3.2 km/sec. The figure is a plot of  $\left(\frac{N}{(kL)^2}\right)$  vs  $\frac{t}{L}$  where N is the total number of

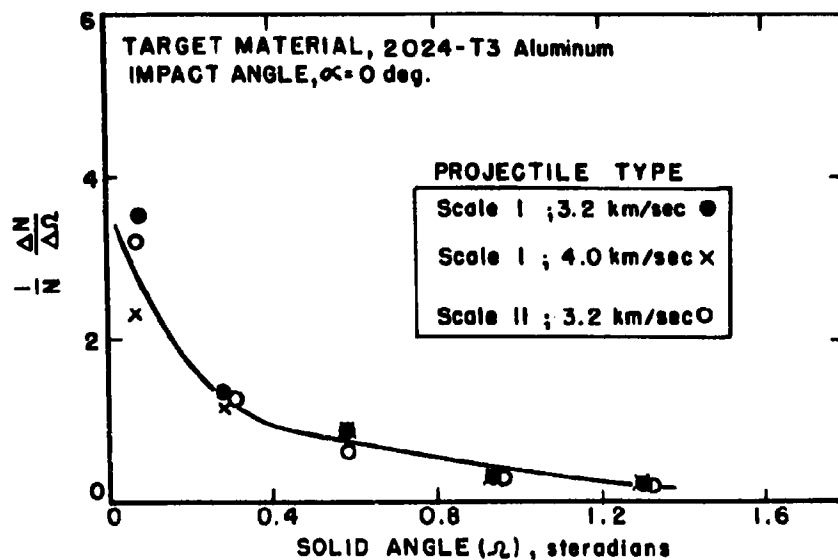


FIGURE 10. - Normalized Distribution for Target Spall Particles.

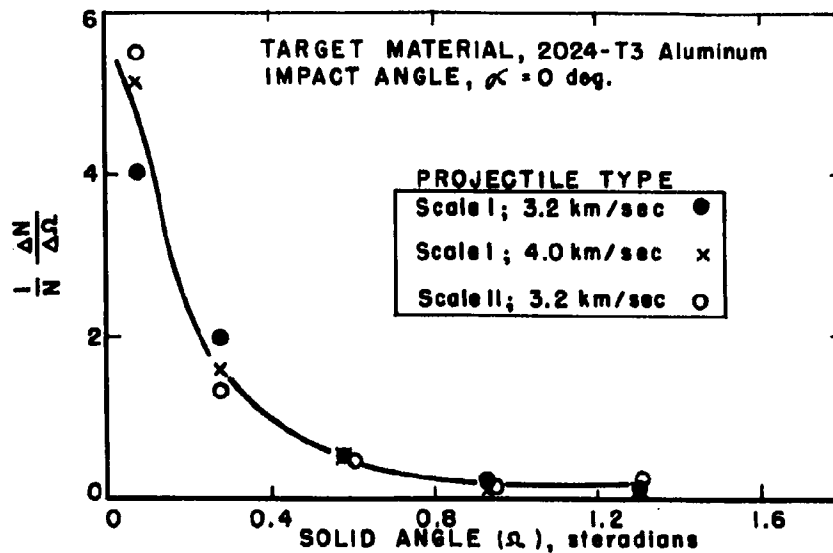


FIGURE 11. - Normalized Distribution for Projectile Remnants.

target spall fragments,  $t$  is the target thickness,  $L$  is the length of the projectile, and  $k$  is a constant such that  $kL = 1$  for the smaller scale size projectile. This treatment is intended to bring the Scale II data points into coincidence with corresponding Scale I data points. The fact that the second power of  $kL$  tends to accomplish this purpose demonstrates that there is a strong tendency for the total number of target spall particles to vary directly with the area of the projectile; this is the case, however, only if the ratio of target thickness to projectile length remains constant.

A somewhat similar treatment is used to demonstrate the scaling effect for the number of projectile remnants produced. These data are presented in figure 13 which shows  $\left(\frac{N}{(kL)^3}\right)$  vs  $\frac{t}{L}$  where  $N$ , in this case, is the total number of projectile remnants. The interpretation here is that the number of projectile remnants produced varies directly with the volume of the projectile, providing the target thickness is scaled with a linear dimension of the projectile.

Data associated with the distributions of numbers of spall particles resulting from oblique impacts on targets have also been obtained. Although a number of significant features of the phenomena are evident, the oblique impact data do not permit as simple an interpretation as data from normal impacts. The added complexities are understandable inasmuch as the center of spall impact does not lie on a line beneath the perforation perpendicular to the target nor on the original line of flight of the projectile; it is found to lie between

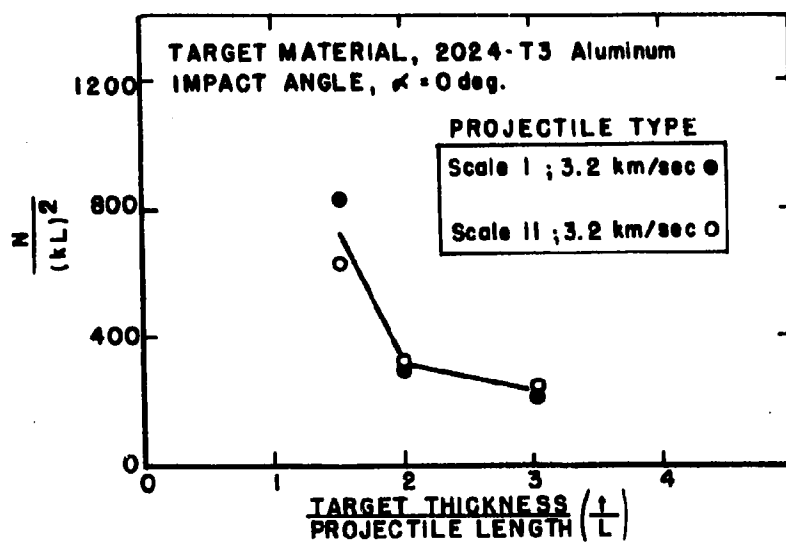


FIGURE 12.- Effect of Projectile Size Upon the Number of Target Spall Particles.

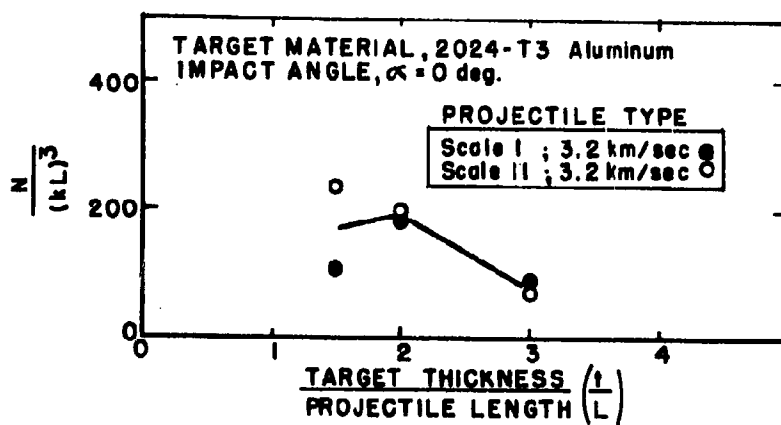


FIGURE 13.- Effect of Projectile Size Upon the Number of Projectile Remnants.

these two extremes. Hence, the distribution of particles, in terms of the target-witness geometry used for normal impacts, is not independent of the azimuthal coordinate  $\phi$  (see figure 8).

The dependence of spall numbers upon the coordinate  $\phi$  is illustrated in figure 14 which is a plot of  $\frac{1}{N} \frac{\Delta N}{\Delta \phi}$  vs  $\phi$  and may be interpreted as representing the percentage of the total number of particles found to reside in indicated intervals of the angular coordinate  $\phi$ . The plot is for data obtained from Scale I projectiles impacting targets at 60 degrees obliquity ( $\alpha = 60$  degrees). Projectile velocities were 2.0 km/sec, 3.2 km/sec, and 4.0 km/sec. The data were averaged for several target thicknesses since, again, a target thickness effect was not apparent. Several significant features of the data are evident: (1) The spall particles are not dispersed symmetrically about the origin of circles on the witness foil (point O in figure 8); rather, the center of spall impact is displaced radially outward along  $\phi = 0$  (in the azimuthal direction corresponding to the line of flight of the projectile). (2) The density of spall particles is maximum along  $\phi = 0$  and diminishes progressively and symmetrically in both the positive and negative angular directions removed from the  $\phi = 0$ . (3) The percentage of the total number of spall particles found in any given element  $\Delta \phi$  is independent of target thickness and projectile velocity. A similar independence for 2S-O aluminum, 24S-O aluminum, and 2024-T3 aluminum for one projectile system (3.2 km/sec, Scale I projectile) was demonstrated earlier (5).

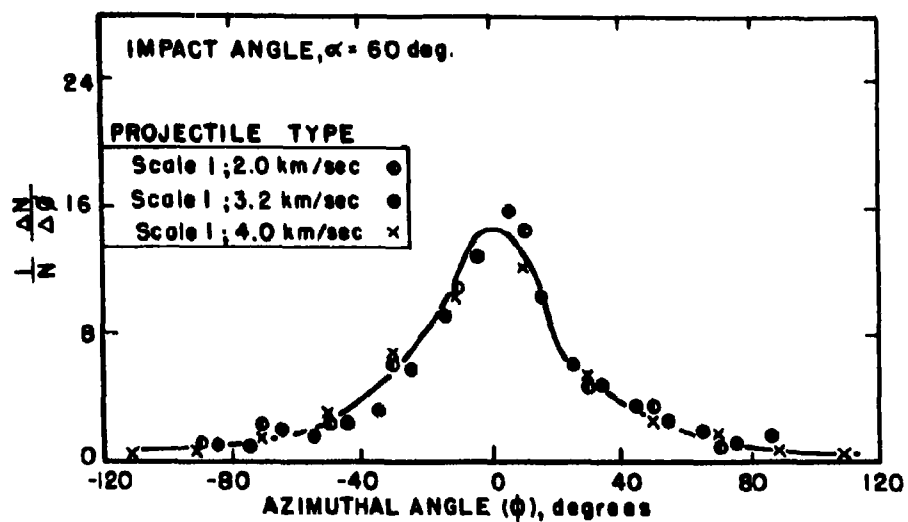


FIGURE 14. - Normalized Population Density as a Function of Azimuthal Angle.

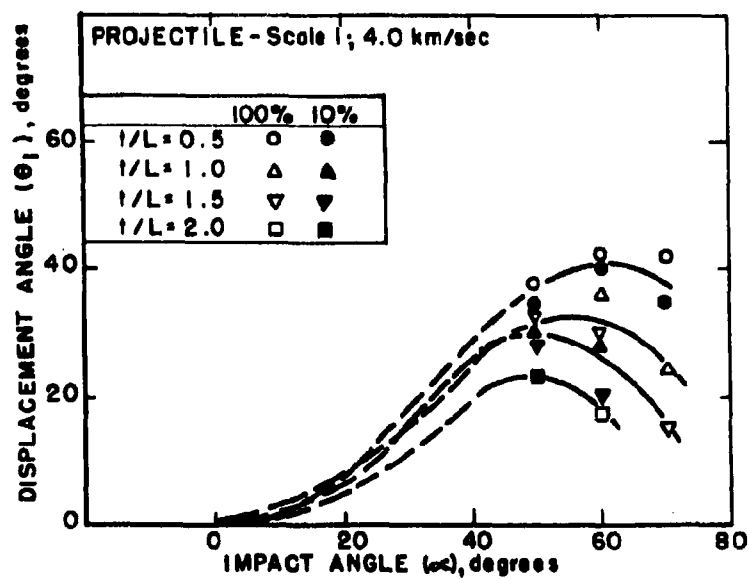


FIGURE 15. - Effect of Impact Angle Upon Displacement Angle.

The displacements of the centers of spall impact as a function of both impact angle and target thickness are plotted in figure 15. The figure is a plot of displacement angle ( $\theta_1$ ) vs impact angle ( $\alpha$ ) with target thickness as a parameter; displacement angle is a measure of the displacement of the center of spall population from point O. The Scale I, 4.0 km/sec projectile, was used to impact 1/32, 1/16, 3/32, and 1/8-inch thick 2024-T3 aluminum targets at 50, 60, and 70 degree impact angles. Target thicknesses are specified relative to the projectile length. An added feature of the plot is that centers of spall populations for the ten percentile group of particles having higher penetration capabilities are shown plotted separately. These data are identified by the designation - 10 percent; the aggregate groups are identified by the designation - 100 percent. Significant features of the plot are as follows: (1) the displacement angle increases with the impact angle up to impact angle values of between 50 degrees and 60 degrees after which a decrease in displacement angle is noted for further increases in impact angle; (2) displacement angle is always less than impact angle; (3) there is a tendency for the ten percentile group to have lower displacement angles; however, the difference is small and for practical purposes they are interpreted to be the same as those for the aggregate group.

It would seem desirable to make a short comment regarding the peculiar behavior noted in (1) above where displacement angle was found to decrease for values of impact angle greater than about 60 degrees. It is believed that the axis for the envelope of projectile remains and associated target particles flowing through the perforation in the target is different from the axis of target spall produced by shock interactions.

The interplay of two such distinct distributions could conceivably cause displacement angle to be a double valued function of impact angle.

### III. Mass Distribution

Mass distribution refers to the manner in which the mass contained in the spall envelope is spatially distributed. The collection agent was gelatin, and the data were derived from the same shots used to determine separate particle population distribution for target spall and projectile remnants. The data are presented in two plots of figures 16 and 17 which show  $\frac{1}{M} \frac{\Delta M}{\Delta \Omega}$  vs  $\Omega$  for the target spall mass and the mass of projectile remnants respectively. The plots contain three data point sets representing Scale I, 3.2 km/sec, Scale I, 4.0 km/sec, and Scale II, 3.2 km/sec projectiles that impacted on various thicknesses of 2024-T3 aluminum targets at normal incidence. Individual data points represent an average for several target thicknesses. Significant features of both plots may be summarized as follows: (1) Both distributions are qualitatively similar to the number distribution plots presented earlier, i.e., maximum density is observed at the center of spall impact and decreases radially outward; (2) the mass distribution for projectile remnants differs from the one for target spall particles in that the former shows a substantially greater percentage of the mass distributed nearer the center of spall impact; similar behavior existed for the number distribution data; (3) the percentage of the total amount of mass (target material or projectile remnants)

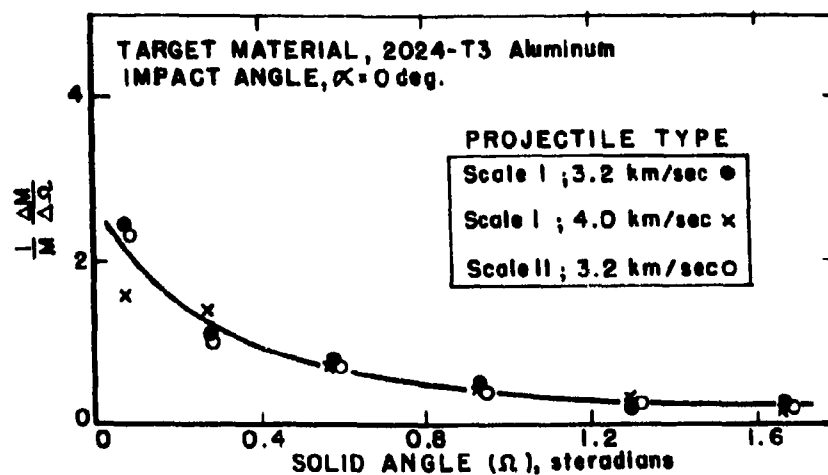


FIGURE 16.-Normalized Distribution for Target Spall Mass.

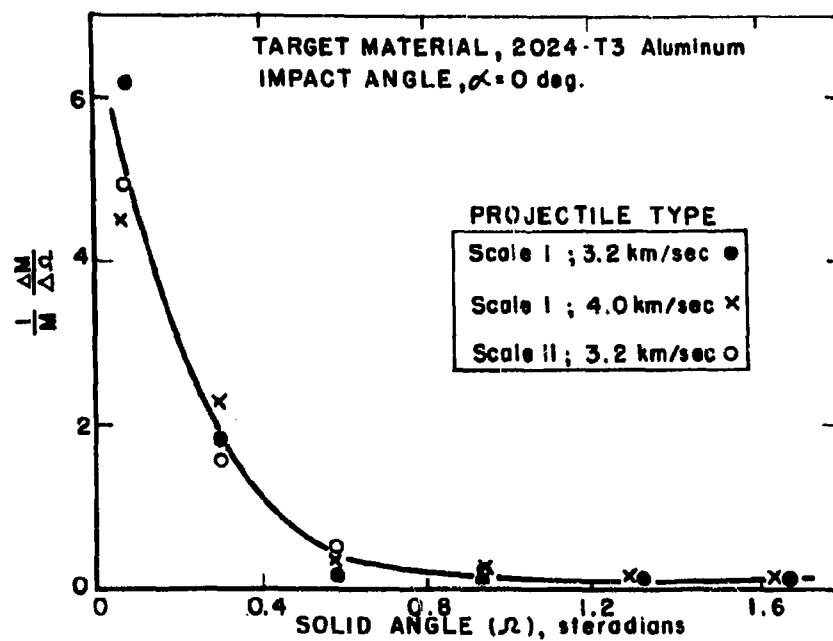


FIGURE 17.-Normalized Distribution for Mass of Projectile Remnants.

found in any given space element is independent of target thickness, projectile scale size, and projectile velocity; (4) from (1) and (2) it may be concluded that particle size is not particularly dependent upon the space coordinates.

Another set of plots, figures 18 and 19, is presented to indicate reasonable scaling laws for the total mass contained in the envelope of material behind thin targets. The graphs show  $\frac{M}{(kL)^3}$  plotted against  $\frac{t}{L}$  for the total target spall mass and the mass of projectile remnants respectively. The power of the quantity  $(kL)$  is three in these instances and indicates that the total spall mass is proportional to the volume of the projectile providing the target thickness is scaled with the linear dimensions of the projectile. The plots also show that the target spall mass increases with target thickness providing one does not closely approach the maximum penetration capability of the projectile; the mass of recovered projectile remains, however, is independent of target thickness at this particular velocity (3.2 km/sec).

Figure 20 shows the effect of target thickness on spall particle size. The plot is presented in terms of the reduced variables  $\frac{1}{kL} \times \text{mass/number}$  vs  $\frac{t}{L}$ . The first power of  $\frac{1}{kL}$  is the proper reducing factor between these Scale I and Scale II impact data because it has been shown that treatment of the mass data involved the third power and the number data the second power of this factor. It should also be pointed out that the values are unweighted average measures of

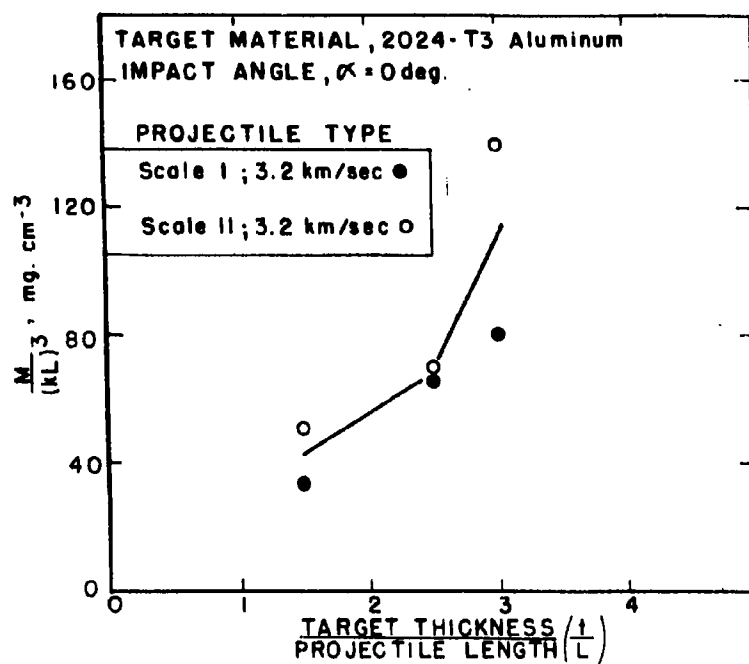


FIGURE 18.- Effect of Projectile Size Upon the Mass of Recovered Target Spall.

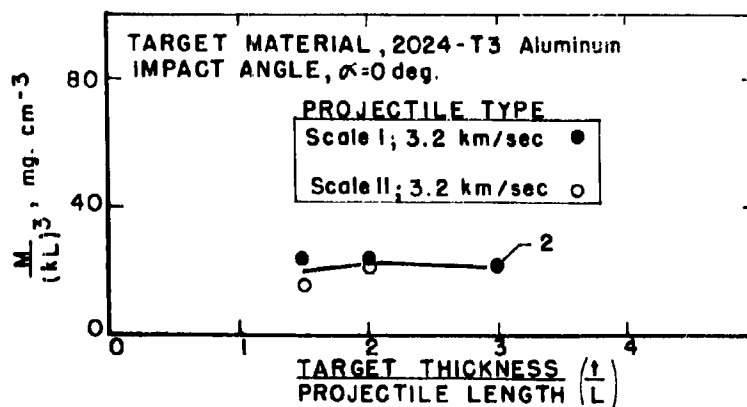


FIGURE 19.- Effect of Projectile Size Upon the Mass of Recovered Projectile Remnants.

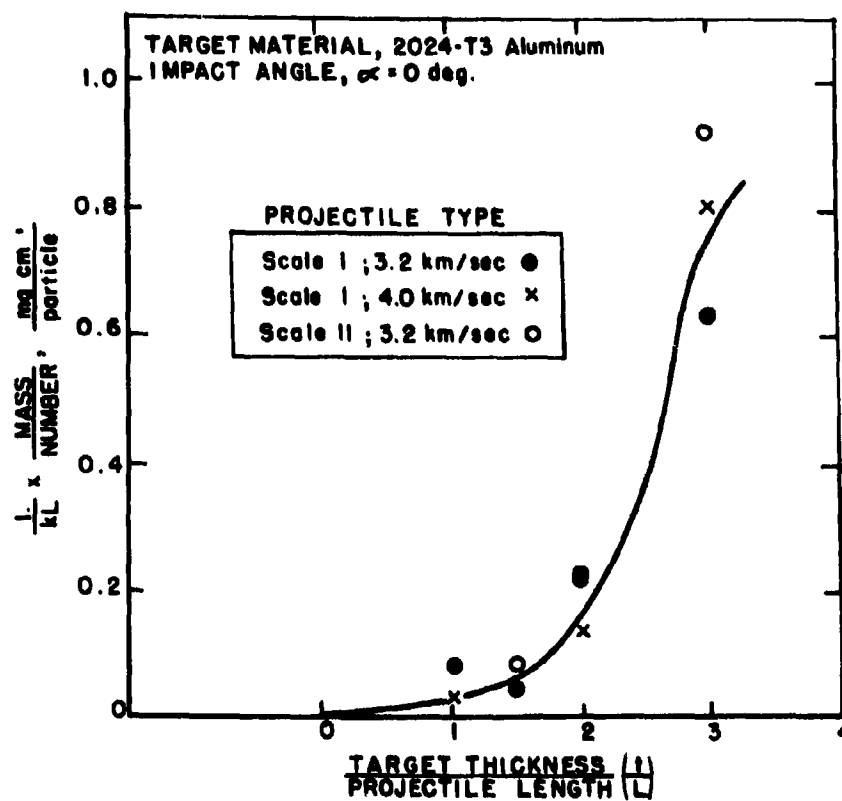


FIGURE 20.—Effect of Target Thickness Upon Average Target Spall Particle Size.

spall particle size because total mass has simply been divided by total number. Individual data point sets are shown for impacts with 3.2 km/sec Scale I, 4.0 km/sec Scale I, and 3.2 km/sec Scale II projectiles. The character of the plot is interesting from several viewpoints: (1) The average size (mass/particle) of the target spall particles increases drastically with increasing target thickness; the increase amounts to almost an order of magnitude for  $\frac{t}{L}$  values ranging from one to three. The change in spall mass and spall numbers with increasing target thickness are in the proper direction for maximum increase in particle size, i.e., spall mass increases while spall numbers decrease. (2) Average spall particle size is proportional to the first power of the scale factor; hence, the Scale II projectiles produce spall particles which are, on the average, twice the size of those produced by Scale I projectiles. (3) The Scale I, 4.0 km/sec data have been included in this plot merely to show that target thickness effect is much more pronounced than the effect from the indicated change in velocity; it is conceivable, however, that a significant velocity effect might be observed if the projectile velocities were substantially different.

#### IV. Velocity Distribution

The experimental effort directed toward a description of the velocity distribution of the material ejected from thin plates was limited by the small scale size of the projection systems used. No

single experiment has proven adequate for this purpose and, as a consequence, several velocity measuring techniques have been employed. A dual-channel flash X-ray system has been successfully applied to the problem of determining the residual velocity of the emerging projectile material. These measurements coupled with target impulse studies, with a ballistic pendulum, have led to values of total target-spall momentum. A recently developed framing camera technique has proven satisfactory for determining the velocity spectrum of the combined projectile and target spall particles produced by a variety of impact conditions. In this technique, the target spall particles and projectile remains are directed toward a thin aluminum foil viewed by the framing camera. The side of the foil away from the camera is uniformly illuminated by means of an exploding wire used in conjunction with a diffusion screen. When the particles puncture the foil, the event is recorded in the framing camera sequence as a bright flash. The time of occurrence of this event relative to the time of target impact and the distance between the target and the witness foil are then used to calculate an average velocity for each particle observed. By an appropriate choice of framing rate the entire velocity spectrum can be mapped.

The results of the investigations carried out in this area are graphically shown in figures 21 through 29; when considered in their entirety they lead to certain conclusions. The formula

$$v_r = \left[ v_o^2 e^{-\frac{\rho_t A_f z}{m_f}} - \frac{2k}{\rho_t} \left( 1 - e^{-\frac{\rho_t A_f z}{m_f}} \right) \right]^{1/2}$$

where  $z$  = instantaneous depth in the target;

$v_r$  = residual fragment velocity;

$A_f$  = cross sectional area of impacting fragment;

$m_f$  = mass of impacting fragment;

$v_o$  = initial fragment velocity;

$\rho_t$  = target density;

$k$  = target strength factor

derived from previous work with 3.2 km/sec, Scale I projectiles (6) is found to be applicable when the projectile scale size is varied. This is illustrated in figure 21 where the measured values of  $v_r$  for both Scale I and Scale II projectiles are plotted as a function of target thickness; a curve calculated from the above formula using the same value of the strength constant  $k$  is also shown.

Furthermore, by reasoning that any net impulse transferred to the target, per se, is due to the forces associated with the strength term,  $k$ , the residual velocity formula can be used to predict target impulse by first calculating the total momentum lost by the projectile in perforating a given target thickness,  $z$ , and then deducting from this value the momentum loss associated with the fluid term in the equation, i.e.,  $k = 0$ . This method was used to obtain the values represented by the curve which is presented in figure 22 along with

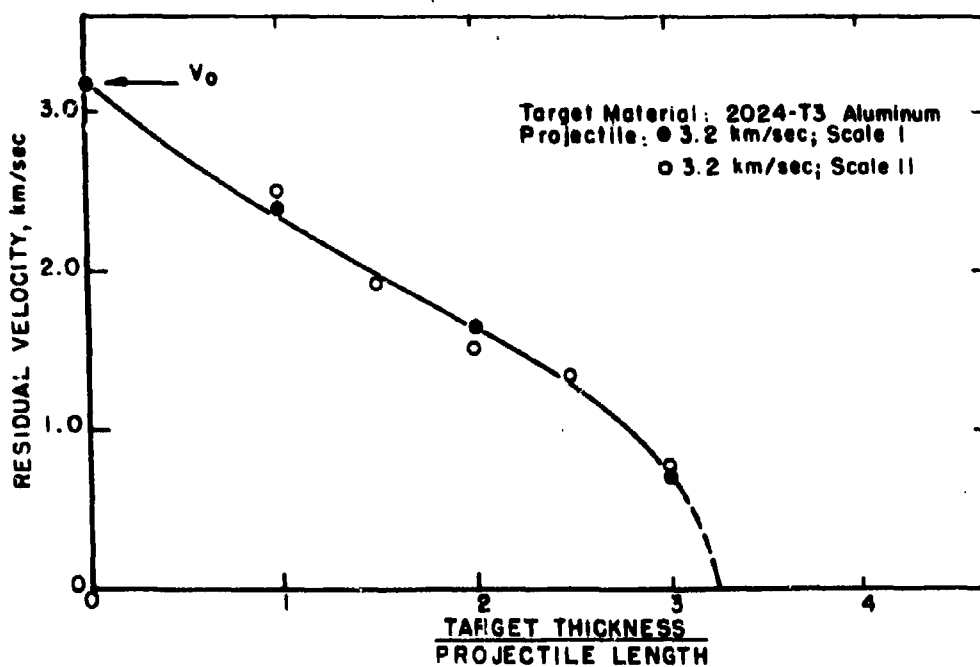


FIGURE 21.—Residual Projectile Velocity as a Function of Target Thickness.

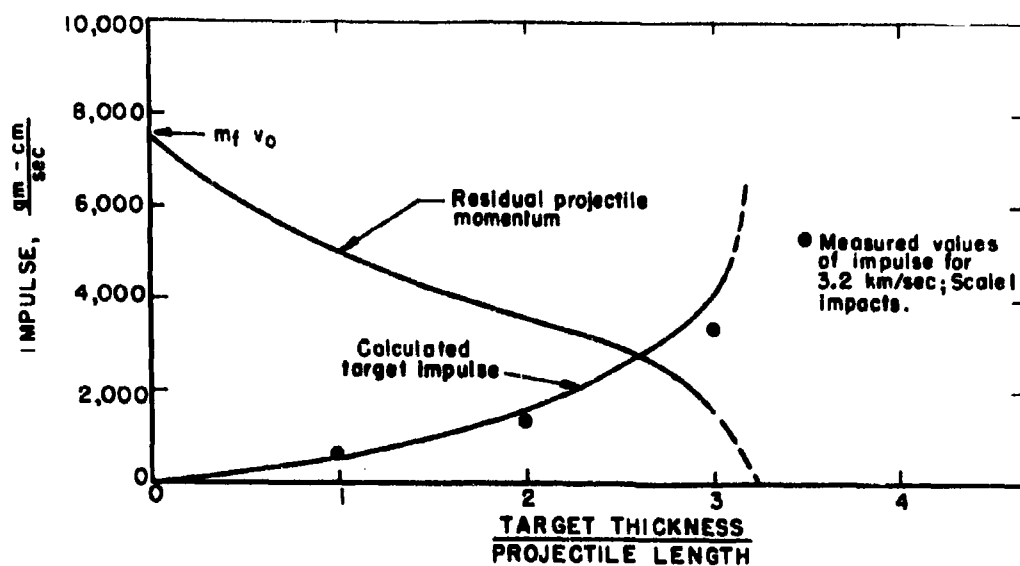


FIGURE 22.—Comparison Between Measured and Calculated Values of Target Impulse.

measured values of target impulse obtained from ballistic pendulum measurements. The agreement between the measured value and the value calculated on the basis of the above model is very good; however, it should be emphasized that the model is based on the assumption that the projectile suffers little deformation during the perforation process. Flash radiographs indicate that this assumption is no longer valid for steel-aluminum impacts above 4 km/sec.

There is, under certain impact conditions, appreciable momentum associated with the material splashed from the front surface of thin targets; consequently, a simple measure of target impulse and a knowledge of projectile momentum is not sufficient for specifying the momentum of the material carried through the target. Stanyukovich has proposed that above a certain critical velocity the momentum delivered to a target structure is simply related to the kinetic energy of the impacting projectile (7).

Specifically, he equates:

$$J = \frac{BE_0}{\sqrt{s}}$$

where  $J$  = total normal impulse;

$E_0$  = projectile energy;

$\sqrt{s}$  = target strength;

$B$  = coefficient of proportionality.

A limited number of tests with aluminum, lead, copper, and cadmium tend to substantiate the above formulation. These results

are presented in figure 23 where the ratio of the total target impulse to the impacting projectile momentum is plotted as a function of reduced impact velocity for a variety of impact conditions. On the assumption that  $\sigma$  represents the shear strength of the target, the above formula can be rewritten as:

$$\frac{J}{J_0} = \frac{B}{2\sqrt{\rho_t}} \frac{v_0}{v_s}$$

where  $J$  = total normal impulse;  
 $J_0$  = projectile momentum;  
 $v_0$  = impact velocity;  
 $\rho_t$  = target density;  
 $v_s$  = shear wave velocity;  
 $B$  = coefficient of proportionality.

Thus, the ratio  $\frac{J}{J_0}$  is a linear function of impact velocity reduced by  $\sqrt{\rho_t} v_s$ . When plotted in this form the data indeed show this linear dependence.

In terms of the thin targets, an interesting and important aspect of the momentum excess phenomenon is illustrated in figure 24 where the experimental results of impulse tests with thin aluminum and lead targets are presented. In these experiments the total forward momentum delivered to the target structure and target spall system was measured as a function of target thickness. For the lead targets,

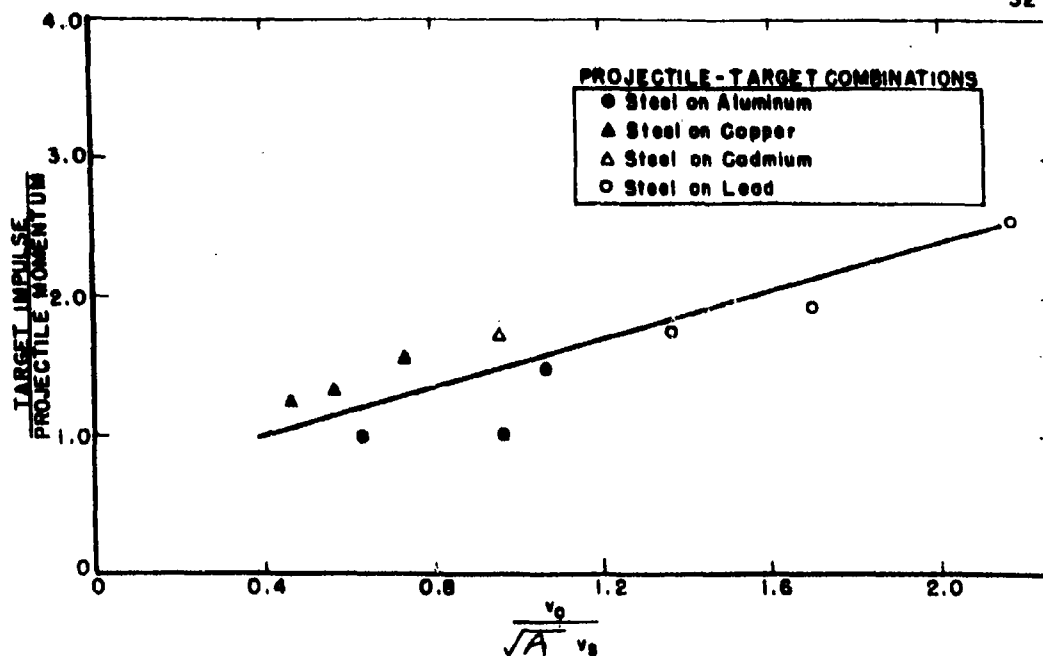


FIGURE 23.-Excess Momentum as a Function of Impact Velocity.

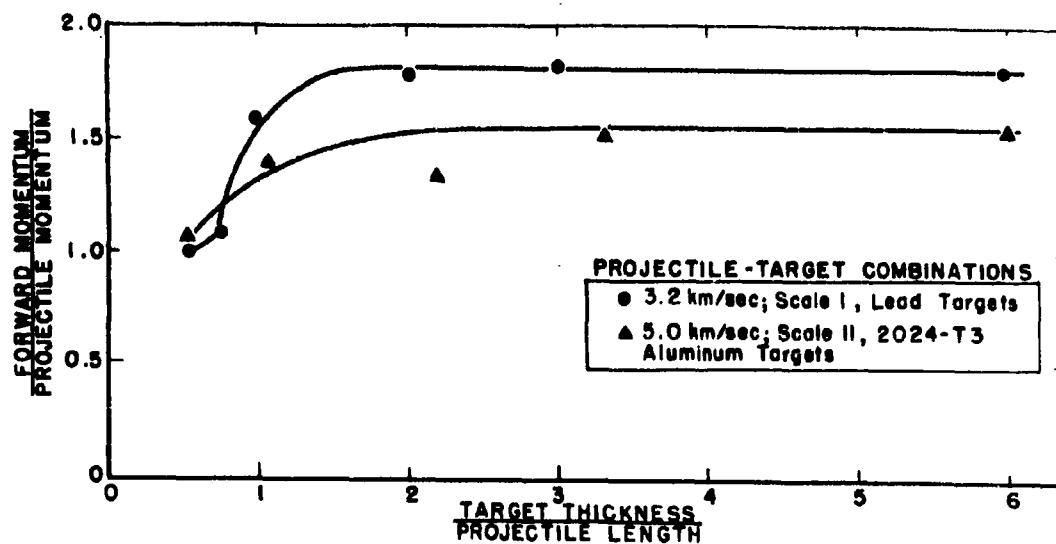


FIGURE 24.-Forward Momentum as a Function of Target Thickness.

3.2 km/sec, Scale I projectiles were used; 5.0 km/sec, Scale II projectiles were used in the aluminum tests since this was the only impact arrangement where excess momentum was observed.

The significant feature of this series of tests is the fact that the total forward momentum is essentially independent of target thickness when the latter exceeds one to two times the projectile length. Since, on the basis of hydrodynamic considerations, these values roughly correspond to the primary penetration expected for these target-projectile combinations, the results indicate that the excess momentum imparted to the target-spall system is derived during the hydrodynamic phase of the perforation process.

The practical implication of these observations is illustrated in figures 25 and 26 where the results of impulse studies in 2024-T3 aluminum targets at impact velocities of 3.2, 4.0, and 5.0 km/sec are summarized. The ratio of target impulse to the initial projectile momentum is plotted as a function of target thickness in figure 25. It will be noted that only a small fraction (20 percent or less) of the total forward momentum is absorbed by the target structure for target thickness less than twice the projectile length.

The ratio of total spall momentum to the initial projectile momentum is plotted in figure 26 as a function of target thickness. These results emphasize the fact that a considerable portion of the total forward momentum is contained in the target ejecta system

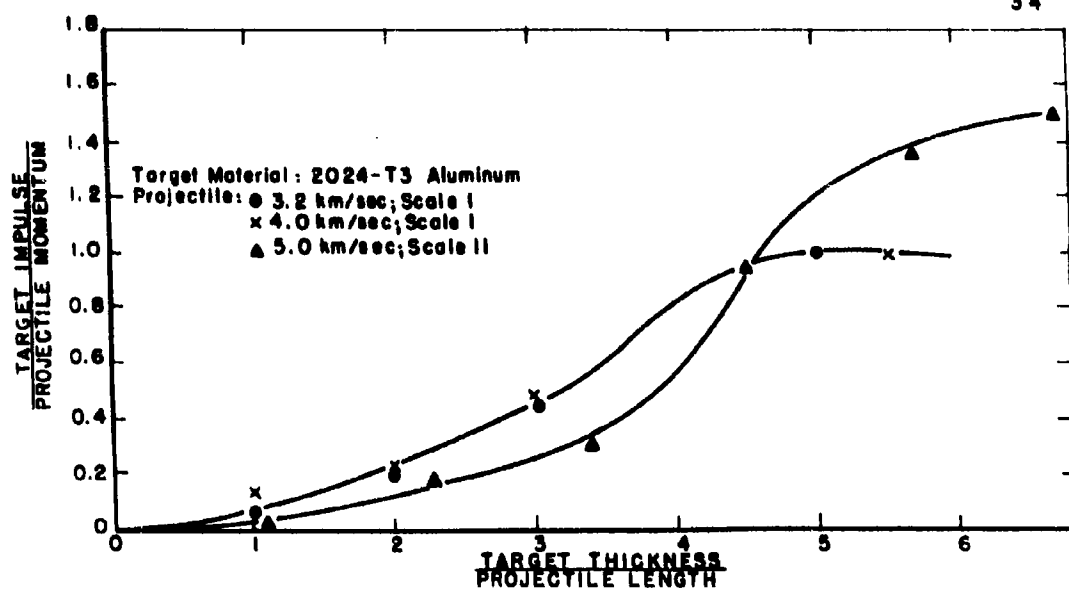


FIGURE 25.-Target Impulse as a Function of Target Thickness.

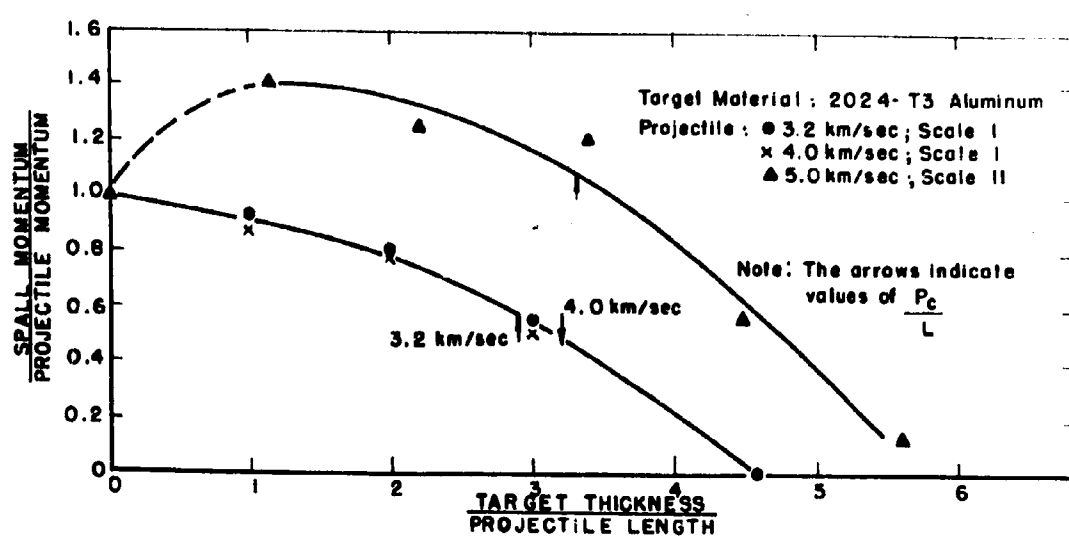


FIGURE 26.-Ejecta Momentum as a Function of Target Thickness.

for target thicknesses in excess of the depth of penetration expected in the semi-infinite target configuration; for impacts at 5.0 km/sec, the value of spall momentum is greater than that of the impacting projectile momentum for target thicknesses equal to or less than  $P_c$  (crater depth in an infinite target).

The framing camera technique has been used to obtain data relative to the velocity distribution of the individual ejecta particles as a function of target thickness for 3.2 km/sec Scale I, 3.2 km/sec Scale II, and 5.0 km/sec Scale II impacts on 2024-T3 aluminum targets. The results of these experiments are presented in figures 27 through 29 where values of  $\frac{\Delta N}{N} \frac{1}{\Delta v}$ , which represent the percentage of the total population lying in a velocity increment  $\Delta v$ , are plotted as a function of velocity for various target thicknesses.

The results indicate that for scaled systems (figures 27 and 28) the velocity distributions are similar in that both the maximum spall velocity (intercepts with the velocity axis) and the maxima of the curves (velocity corresponding to the maximum percentage of the total number) nearly coincide.

The velocity distribution curves for different target thicknesses impacted at 3.2 km/sec and 5.0 km/sec show the expected shift in the direction of lower velocity values as the target thickness is increased. The distributions obtained in 3.2 km/sec and 5.0 km/sec Scale II tests with 3/8 inch thick targets tend to show a bimodal form which probably

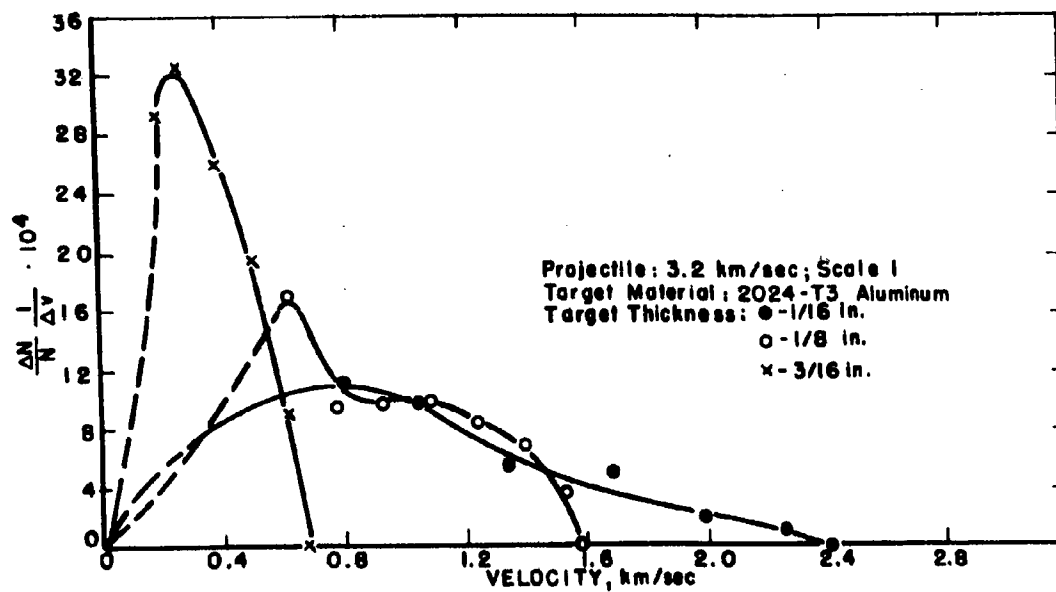


FIGURE 27. - Velocity Distribution of Target Ejecta from 3.2 km/sec Scale I Impacts.

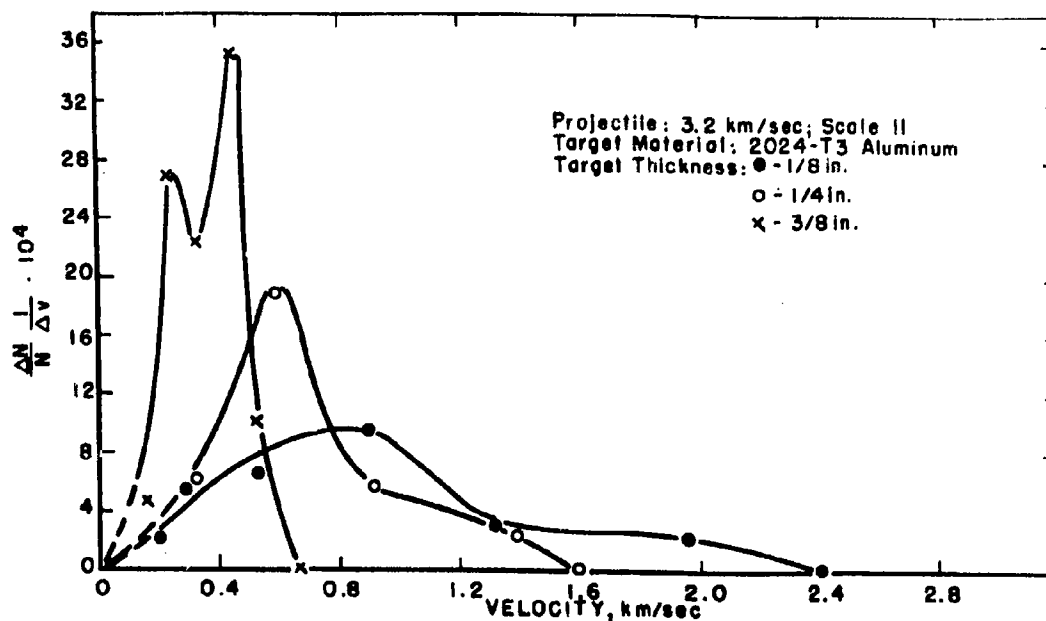


FIGURE 28. - Velocity Distribution of Target Ejecta from 3.2 km/sec Scale II Impacts.

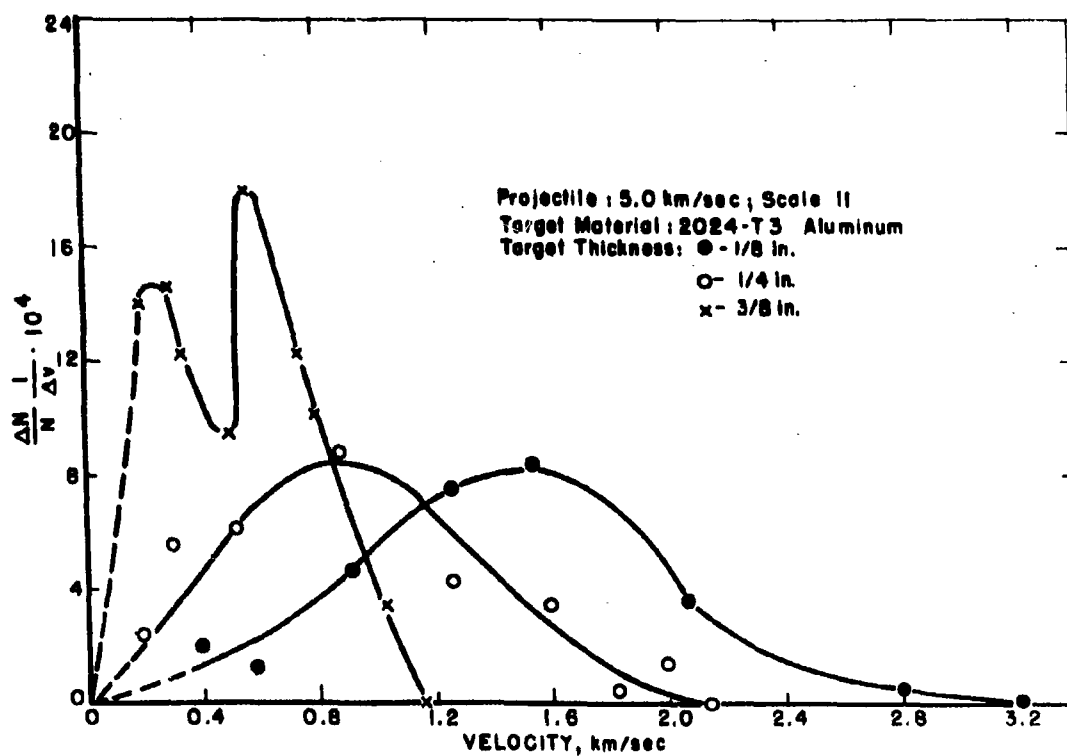


FIGURE 29.— Velocity Distribution of Target Ejecta from 5.0 km/sec Scale II Impacts.

arises from a distinction between the velocities of the projectile remnants (and/or target material driven through the perforation) and spallation resulting from shock interaction at the free surface of the target.

#### CONCLUSIONS

The more important aspects of the thin plate perforation process have been investigated over the velocity range from 2 to 5 km/sec. Particular emphasis was placed on studying the spatial, mass, and velocity distribution of rear surface ejecta as the impact velocity, projectile scale size, and the target thickness were varied. A number of simple relationships have been established among these variables. For the case of a nondeforming projectile, it has been shown that residual projectile velocity and target impulse can be predicted on the basis of a simple mathematical model.

The situation is much more complicated where the projectile is seriously deformed. However, the observations relating to the behavior of the target ejecta system indicate the applicability of a simple-shock-spallation model. Evidence for this comes from the projectile scale size experiments at 3.2 km/sec where it was found that the mass of target material varied with the cube of the characteristic projectile dimension while the total number of target particles generated varied with the square of the projectile dimension. The formation and subsequent breakup of a back surface spall might lead

to these results if proposed spall scaling laws are valid (8). In addition, the number of target particles is found to depend heavily on target thickness, decreasing markedly as the target thickness is increased. Furthermore, for a given target thickness and projectile scale size, the number of particles is found to increase with impact velocity. This behavior suggests that the number of particles generated in any given impact situation depends primarily on the intensity of the shock wave incident on the rear surface of the target. The general behavior of the velocity distributions of the ejecta can be described in these same terms.

Further evidence supporting the proposed spall model lies in the observed insensitivity of the spatial distributions of the target ejecta on any of the experimental parameters. Since the ratio of the radial and normal components of velocity of a given particle would depend heavily on the curvature of the impinging shock wave (a slowly varying function of the initial parameters) rather than the incident shock strength (a rapidly varying function of the initial parameters), this observation is also compatible with the proposed model.

## REFERENCES

1. Watson, R. W., K. R. Becker, G. M. Bryan, and R. Vitali. Fundamentals of Shaped Charges, Carnegie Institute of Technology, Contract No. DA-36-061-ORD-513, October 31, 1961, pp. 2-12.
2. Kineke, John H. Jr., and Lee S. Halloway. Macro-Pellet Projection with an Air Cavity High Explosive Charge for Impact Studies, BRL Memorandum Report No. 1264, April 1960, 17 pp.
3. Atkins, W. W. Hypervelocity Penetration Studies. Proc. of Fourth Hypervelocity Impact Symposium, April 26-28, 1960.
4. Kineke, John H. Jr. An Experimental Study of Crater Formation in Metallic Targets. Proc. of Fourth Hypervelocity Impact Symposium, April 26-28, 1960.
5. Vitali, R., K. R. Becker, and R. W. Watson. Perforation of Finite Targets by High Velocity Projectiles. Proc. of Fifth Symposium on Hypervelocity Impact, Vol. 1, Part 2, April 1962, pp. 595-596.
6. Watson, R. W. Perforation of Thin Plates by High Velocity Fragments. Proc. of Fifth Symposium on Hypervelocity Impact, October 1961, pp. 587-588.
7. Stanyukovich, K. P. Concerning the Impact of Solids at High Velocities. J. Exptl. Theoret. Phys. (U.S.S.R.) 36, May 1959, pp. 1605-1606.
8. Erkman, John O. Decay of Explosivity-Induced Shock-Waves in Solids and Spallings of Aluminum. Third Symposium on Detonation, Princeton University, September 26-28, 1960, pp. 253-266.

**DISTRIBUTION LIST FOR**

**Type I Quarterly Report**

**on**

**Hypervelocity Impact Phenomena**

**Sponsored by the Department of the Army  
Aberdeen Proving Ground**

Commanding General  
Aberdeen Proving Ground  
Maryland  
Attn: F. E. Allison  
Ballistic Research Laboratories

Commanding General  
Aberdeen Proving Ground  
Maryland  
Attn: R. J. Eichelberger  
Ballistic Research Laboratories

Commanding General  
Aberdeen Proving Ground  
Maryland  
Attn: Technical Library  
Ballistic Research Laboratories

Office, Chief of Ordnance  
Department of the Army  
Washington 25, D. C.  
Attn: ORDTU

British Joint Services Mission  
1800 K Street, N. W.  
Washington 6, D. C.  
Attn: Reports Officer

Commanding Officer  
U. S. Naval Ordnance Test Station  
China Lake, California  
Attn: J. W. Rogers

Commanding Officer  
Air Proving Ground Center  
Eglin Air Force Base, Florida  
Attn: H. L. Davis

Commanding General  
Aberdeen Proving Ground  
Maryland  
Attn: S. Kronman  
Ballistic Research  
Laboratories

Commanding General  
Aberdeen Proving Ground  
Maryland  
Attn: J. Kneke  
Ballistic Research  
Laboratories

Office, Chief of Ordnance  
Department of the Army  
Washington 25, D. C.  
Attn: ORDTB, Ballistics Section  
Mr. M. C. Miller

Commanding Officer  
Armed Services Technical  
Information Agency  
Arlington Hall Station  
Arlington 12, Virginia  
Attn: TIPCR

Canadian Army Staff  
2450 Massachusetts Avenue  
Washington 8, D. C.

Director  
U. S. Naval Research Laboratory  
Washington 25, D. C.  
Attn: Mr. W. W. Atkins, Code 130

Commanding Officer  
Air Proving Ground Center  
Eglin Air Force Base, Florida  
Attn: Lt. W. H. Ditttrich  
Det. 4, ASD(ASQWR)

Director, The RAND Corporation  
1700 Main Street  
Santa Monica, California  
Attn: J. H. Huth

Director, The RAND Corporation  
1700 Main Street  
Santa Monica, California  
Attn: R. L. Bjork

Director, The RAND Corporation  
1700 Main Street  
Santa Monica, California  
Attn: Technical Library

Library of Congress  
Technical Information Division  
Reference Department  
Washington 25, D. C.  
Attn: Bibliograph Section

General Motors Corporation  
Defense Systems Div., Box T  
Santa Barbara, California  
Attn: J. W. Gehring

The Firestone Tire & Rubber Company  
1200 Firestone Parkway  
Akron, Ohio  
Attn: C. M. Cox

Commanding Officer  
Air Proving Ground Center  
Eglin Air Force Base, Florida  
Attn: F. E. Howard  
Det. 4, ASD(ASQP)

Director, National Aeronautics &  
Space Administration  
Ames Research Center  
Moffett Field, California  
Attn: J. L. Summers

Director, National Aeronautics &  
Space Administration  
Ames Research Center  
Moffett Field, California  
Attn: Technical Library

Director, National Aeronautics &  
Space Administration  
Langley Research Center  
Langley Field, Virginia  
Attn: W. H. Kinard

Director, National Aeronautics &  
Space Administration  
Langley Research Center  
Langley Field, Virginia  
Attn: Technical Library

General Motors Corporation  
Defense Systems Div., Box T  
Santa Barbara, California  
Attn: Technical Library

Aeroelastic & Structures  
Laboratory  
Massachusetts Institute of  
Technology  
77 Massachusetts Avenue  
Cambridge 39, Massachusetts  
Attn: W. Herrmann

Drexel Institute of Technology  
Mechanical Engineering Dept.  
Philadelphia 4, Pennsylvania  
Attn: Pei Chi Chou

National Aeronautics and Space  
Administration  
Lewis Research Center  
21000 Brookpark Road  
Cleveland 35, Ohio

General Atomic Division  
General Dynamics Corporation  
P. O. Box 608  
San Diego, California  
Attn: J. M. Walsh

General Atomic Division  
General Dynamics Corporation  
P. O. Box 608  
San Diego, California  
Attn: M. F. Scharff

Pratt and Whitney Aircraft Division  
United Aircraft Corporation  
East Hartford, Connecticut  
Attn: H. Kraus

Flight Physics Laboratory  
Defense Research Laboratory, Box T  
General Motors Corporation  
Santa Barbara, California  
Attn: A. B. Wenzel